Journal of Biomedical Optics

SPIEDigitalLibrary.org/jbo

Optimization of confocal scanning laser ophthalmoscope design

Francesco LaRocca
Al-Hafeez Dhalla
Michael P. Kelly
Sina Farsiu
Joseph A. Izatt

SPIE

Optimization of confocal scanning laser ophthalmoscope design

Francesco LaRocca,[a] Al-Hafeez Dhalla,[a] Michael P. Kelly,[b] Sina Farsiu,[b,a] and Joseph A. Izatt[a,b]
[a]Duke University, Department of Biomedical Engineering, Durham, North Carolina 27708
[b]Duke University Medical Center, Department of Ophthalmology, Durham, North Carolina 27710

Abstract. Confocal scanning laser ophthalmoscopy (cSLO) enables high-resolution and high-contrast imaging of the retina by employing spatial filtering for scattered light rejection. However, to obtain optimized image quality, one must design the cSLO around scanner technology limitations and minimize the effects of ocular aberrations and imaging artifacts. We describe a cSLO design methodology resulting in a simple, relatively inexpensive, and compact lens-based cSLO design optimized to balance resolution and throughput for a 20-deg field of view (FOV) with minimal imaging artifacts. We tested the imaging capabilities of our cSLO design with an experimental setup from which we obtained fast and high signal-to-noise ratio (SNR) retinal images. At lower FOVs, we were able to visualize parafoveal cone photoreceptors and nerve fiber bundles even without the use of adaptive optics. Through an experiment comparing our optimized cSLO design to a commercial cSLO system, we show that our design demonstrates a significant improvement in both image quality and resolution. [DOI: 10.1117/1.JBO.18.7.076015]

Keywords: scanning laser ophthalmoscopy; optical design; optimization.

Paper 130135R received Mar. 8, 2013; revised manuscript received Jun. 15, 2013; accepted for publication Jun. 17, 2013; published online Jul. 17, 2013.

1 Introduction

The confocal scanning laser ophthalmoscope (cSLO) is capable of producing high-contrast retinal images by raster scanning a laser spot and detecting backscattered light through a confocal pinhole.[1–3] High-contrast images are achieved because both the method of raster scanning and the use of a confocal pinhole allow for the minimization of optical cross talk, defined as unwanted light scattered from areas outside the focal volume.[4]

cSLO systems have been widely adapted for various clinical applications. The earlier diagnostic applications of cSLO included detection of the imaging biomarkers of diabetic retinopathy,[5] age-related macular degeneration,[6] and glaucoma.[7] More recent generations of cSLO have enhanced and extended application of this imaging modality. For example, ultra-wide-field scanning laser ophthalmoscopes are used to evaluate ischemia in retinal diseases such as retinal vein occlusion.[8] On another front, combined imaging of cSLO and spectral-domain optical coherence tomography (OCT) with separate[9] or shared[10] light sources has been demonstrated for enhanced image aiming, guidance, and motion tracking as well as optimal classification of disease imaging biomarkers. Finally, integration of adaptive optics with cSLO has enabled visualization of individual cone photoreceptors including those at the fovea where they are most closely packed,[11–13] and more recently rod photoreceptors,[14] which are smaller than foveal cone photoreceptors. Many of these exciting advances in cSLO application are achieved with relatively more expensive, complex, and larger-footprint designs (especially in the case of adaptive optics-based-systems). However, with less expensive, nonadaptive optics cSLO designs, several groups have been able to visualize cone photoreceptors, albeit with lesser resolution, in subjects with good eye optics, and sufficiently far away from the fovea.[15–19] In this paper, we describe a low-cost, compact, nonadaptive optics, lens-based cSLO design that maximizes performance parameters such as field of view (FOV) and throughput while maintaining the resolution necessary to visualize cone photoreceptors as close to the fovea as possible without correcting for ocular aberrations.

One of the guiding principles behind the original design of the SLO is the inversion of the allocation of pupils according to the Gullstrand principle.[3] In order to avoid strong artifactual reflections from the cornea, typical fundus cameras illuminate the retina through an annular aperture imaged into the pupil, while collecting reflected light only through the small central spot. On the other hand, the SLO illuminated through a small central portion of the pupil and collected over the entire remaining pupil. This allowed for much greater light collection efficiency while simultaneously reducing cross talk, and the cSLO further increased resolution and contrast through confocality. In our design described below, we employ a pupil configuration similar to the original SLO except that we illuminate through a larger portion of the pupil and collect over the entire pupil.

Although methods for building a functional cSLO[1–3] or an optimized mirror-based adaptive optics scanning laser ophthalmoscope (ASOLO)[20,21] have been described in the literature, procedures for optimizing a lens-based cSLO optical design based on balancing fundamental optical trade-offs have not been addressed. In what follows, we first present fundamental cSLO design equations and describe their use in arriving at a first-order design. Next, we explain and characterize our detailed lens-based optical design that achieves near diffraction-limited resolution with minimized imaging artifacts. Finally, we show

Address all correspondence to: Francesco LaRocca, Duke University, 136 Hudson Hall, Box 90281, Durham, North Carolina 27708. Tel: 919-660-2475; Fax: 919-613-9144; E-mail: fl20@duke.edu

the imaging results of an experimental implementation of our cSLO design. These results include a study measuring the relationship between throughput and sharpness as a function of pinhole size and a comparison between images taken from our optimized cSLO design and a commercial cSLO system.

2 Methods

2.1 *cSLO Design Parameters*

A generalized cSLO design is shown in Fig. 1 which is useful for deriving basic relationships between design parameters and cSLO performance. The generalized design includes separate optical pathways for illumination and collection through a common telescope whose function is to image the subject's pupil plane into the optical scanner aperture. Although practical cSLOs utilize paired scanners to construct a two-dimensional raster scan, it is typically the faster scanner which limits performance due to electro-mechanical trade-offs between scan frequency, scanner aperture, and maximum scan angle.[22,23] Thus, we only include the limiting (i.e., fast) scan direction here and assume that the slow scanner is either placed close to or imaged onto it by use of a second telescope.

Fundamental cSLO performance parameters considered include the maximum FOV, optical throughput (T), frame rate (FR), and resolution. Note that the maximum FOV parameter corresponds to the maximum square FOV since it is very likely that the slow scanner can match and even exceed the maximum scan range of the fast scanner. These performance parameters depend upon design parameters such as the subject eye's pupil diameter (P), the cSLO telescope magnification (M), the pinhole size (PH), and the limiting scanner parameters, which are the fast scanner aperture (D), maximum optical scan angle (θ), and scan repetition frequency (freq). These basic parameters and components of the cSLO design are shown and labeled in the generalized cSLO schematic in Fig. 1.

The maximum one-dimensional FOV of the cSLO entering the eye is a function of the maximum optical scan angle and telescope magnification. Telescopes that de-magnify the object size also magnify scan angles, so the maximum FOV can be described as simply the maximum optical scan angle after angular magnification:

$$\mathrm{FOV} = M \cdot \theta. \tag{1}$$

The throughput of the cSLO is a function of the limiting (fast) scanner aperture and the collection beam diameter ($M \cdot P$), which is in turn limited by the size of the pupil imaged by the telescope into the scanner plane. Reflected light which makes it back through the pupil but overfills the scanner aperture is clipped, reducing throughput, and exposing the subject to unnecessary light exposure. We quantify throughput as the ratio of the fast scanner aperture and the collection beam diameter:

$$T = \frac{\text{Fast scanner aperture}}{\text{Collection beam diameter}} = \frac{D}{M \cdot P}. \tag{2}$$

Interestingly, taking the product of throughput and maximum FOV gives an expression proportional to the scan-angle mirror-size product for the fast scanner ($\theta \cdot D$) [Eq. (3)]. Thus, the optimal fast scanner for cSLOs is one with the largest scan-angle mirror-size product at a given scanning frequency:

$$\mathrm{FOV} \cdot T = \frac{M \cdot \theta \cdot D}{M \cdot P} = \frac{\theta \cdot D}{P}. \tag{3}$$

The frame rate of the cSLO is limited by the desired number of lines per frame and the number of lines per unit time, which in turn is related to the scanning frequency of the fast scanner. If only one sweep of the fast scanner is acquired, the number of lines per unit time is equal to the scanning frequency. If both front and back sweeps are acquired, the number of lines per unit time is twice the scanning frequency. The frame rate is then the ratio of the number of lines per unit time and the number of lines per frame:

$$\mathrm{FR} = \frac{\text{lines per unit time}}{\text{lines per frame}} = \frac{(1\text{or}\,2) \times \text{freq}}{\text{lines per frame}}. \tag{4}$$

The cSLO, like any linear imaging system, has a resolution that can be described by the full width at half maximum intensity (FWHM) of the intensity point-spread function (PSF) of the detected light from a point source object.[24] More specifically, the theoretical resolution of the cSLO can be described similarly to that of a confocal scanning laser microscope[25] because the cSLO is a confocal scanning laser microscope that uses the patient's eye as the objective lens.[26] Thus, the equation for the PSF at the detector plane of the cSLO ($\mathrm{PSF_{det}}$) can be described as

$$\mathrm{PSF_{det}} = \mathrm{PSF_{illum}} \times (\mathrm{PSF_{coll}} \otimes \mathrm{PH}), \tag{5}$$

where $\mathrm{PSF_{illum}}$ is the PSF of the illumination optics including the eye, $\mathrm{PSF_{coll}}$ is the PSF of the collection optics including

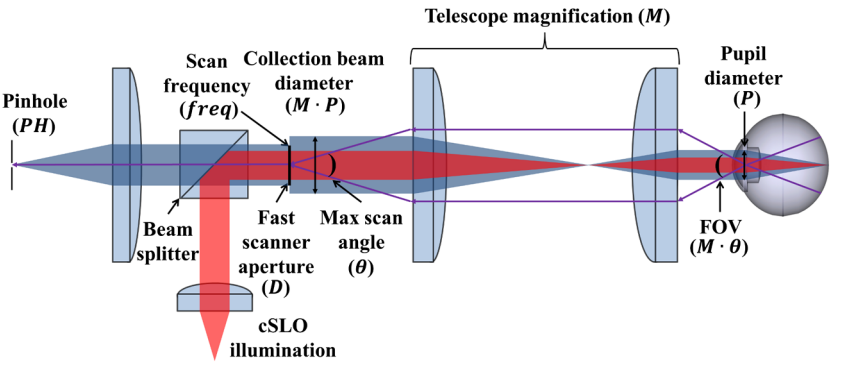

Fig. 1 Generalized one-dimensional schematic of confocal scanning laser ophthalmoscope (cSLO) design showing both the illumination path (red) and collection path (blue) for zero scan angle. The purple lines indicate the chief rays of the optical return path at the extrema of the scan angle.

the eye and scattering properties of the retina, and PH is a function that represents the transmission through the confocal pinhole of a certain size, shape, and position. Due to the direction-sensitivity of light reflected from retinal photoreceptors (referred to as the optical Stiles–Crawford effect), the pinhole size, shape, and position can be designed to relatively increase the amount of signal from the photoreceptor layer thus improving photoreceptor visualization.[27–29]

2.2 *First-Order Design Procedure*

The design procedure of our cSLO was driven by seven constraints that we set based on our desired application: a compact, low-cost, lens-based cSLO system. The inputs/constraints and the resulting design decisions are presented in the diagram in Fig. 2.

To make our system as compact as possible, we chose to use a combination of a resonant scanner and galvanometer with the scanners placed as close as to each other as mechanically possible without risking damage to the scanners (~8 mm separation). To minimize system cost, we chose to use off-the-shelf optics, to electronically filter with a low-cost, custom-fabricated amplifier, and to detect with an avalanche photodiode (APD) instead of a photomultiplier tube. To achieve 8 frames per second (fps) imaging speed with 500 lines per frame, we used a 2-kHz resonant scanner (Electro-Optical Products Corp., Glendale, New York, USA) and utilized both sides of the scan sweep to effectively scan at 4 kHz. The 2-kHz resonant scanner had a 20-deg peak-to-peak maximum optical scan range with an aperture size of 10×10 mm and a limiting aperture (D) of 7 mm due to the 45-deg tilt of the scanner. To maximize throughput ($T = 1$) we used the expression for throughput (T) in Eq. (2) and solved for the magnification of the telescope (M) assuming a maximum (dilated) pupil diameter of the eye (P) to be 7 mm. This gave a design magnification (M) of 1. Using this magnification, we determined that the FOV of our system would be 20 deg from Eq. (1). To maximize lateral resolution on the retina, we chose to use a 2.5-mm illumination beam diameter at the pupil of the eye, which was determined to be the optimal beam diameter for lateral resolution based on the aberrations of 15 subjects as described by Donnelly and Roorda.[30] This illumination beam diameter infers an Airy disk radius at the retina (assuming ideal ocular optics) of 7 μm.

2.3 *Optimized Optical Design*

We optimized the cSLO optical design using Zemax to achieve near diffraction-limited resolution across a 20-deg FOV. Achromatic doublet lenses were used to minimize chromatic aberration and lens splitting was utilized after the scanners to reduce spherical aberration. An effective focal length of 50 mm was chosen for each set of lenses in the cSLO telescope to balance device size and aberrations. The corneal reflection was minimized by constraining the system design such that the specular reflection from the cornea–air interface was well out of focus at the plane of the confocal pinhole; thus, strongly rejecting this backscattered light. Lens reflections were not optimally minimized through the optics since they are stationary with the system and did not saturate the detector, amplifier, or digitizer and so could be removed through background subtraction.

An overview of the optimized optical design of our cSLO is shown in Fig. 3. Spot diagrams, modulation transfer function plots, and an off-axis PSF plot were determined using a recent eye model from Goncharov and Dainty[31] and are shown in Figs. 4, 5(a), and 5(b), respectively. The PSF plot was of a configuration demonstrating the largest FWHM of 7 μm. A fixation

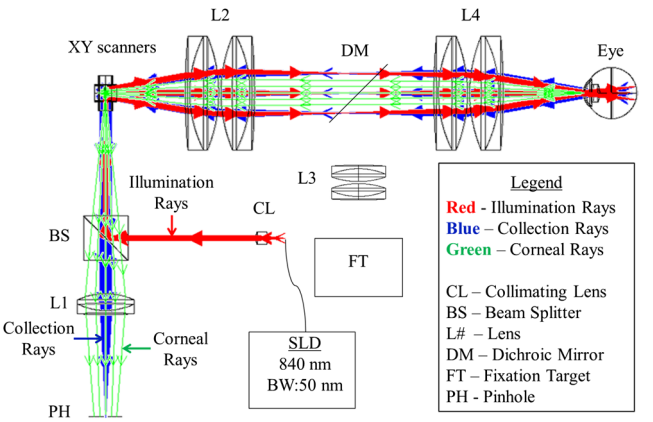

Fig. 3 Schematic of the optimized cSLO as described in the text with the confocal pinhole at the end of the optical path from the eye with the illumination input (red), backscattered collection of light from the retina (blue), and backscattered light from the cornea (green).

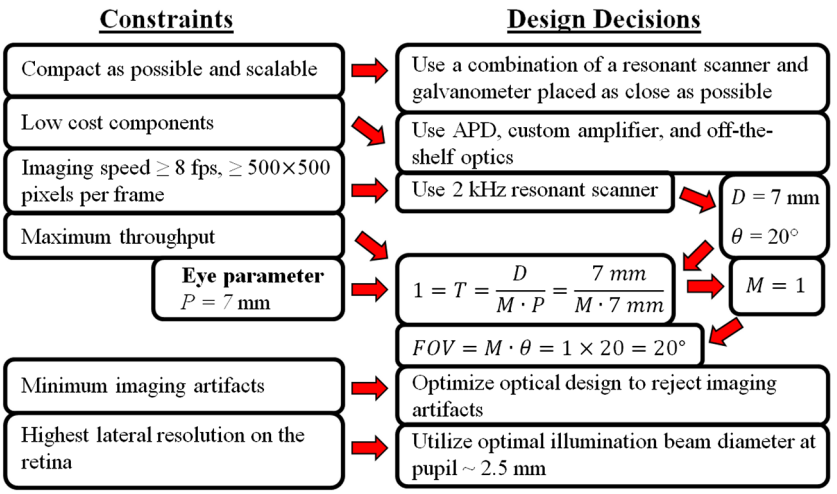

Fig. 2 First-order design procedure for compact cSLO design.

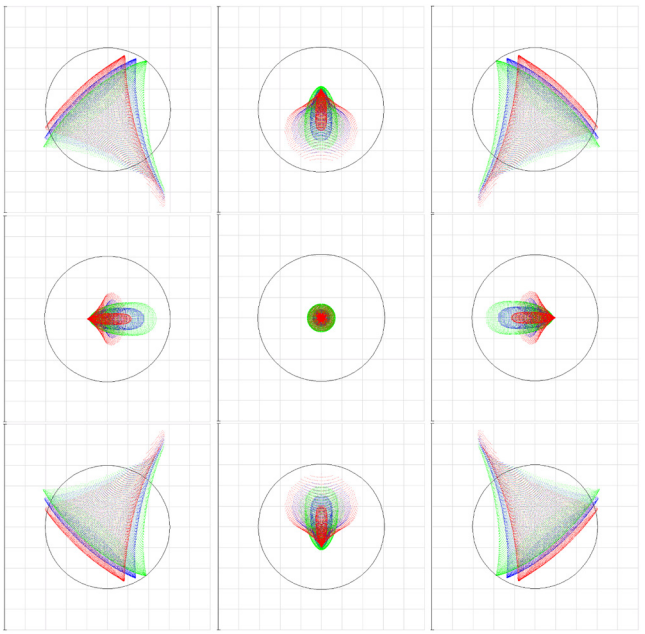

Fig. 4 Object plane spot diagrams for nine configurations spanning a 20-deg field of view (FOV) square on the Goncharov and Dainty[31] model eye's retina demonstrating near diffraction-limited resolution for the illumination path. The Airy disk radius was 7 μm. The Strehl ratios for the center, top-bottom, left-right, and corner configurations are 0.981, 0.975, 0.944, and 0.674, respectively.

target to minimize patient eye motion was inserted by placing a dichroic mirror between the last two sets of lenses before the eye (see Fig. 3) in order to image the fixation pattern displayed by a 1 in. liquid crystal display (LCD) screen onto the retina. The lens closest to the eye was mounted on a knob-adjustable rack-and-pinion linear translator designed to allow for ± 6 diopters of refraction correction. A photograph of the implemented cSLO design is shown in Fig. 6.

The cSLO source was a superluminescent diode (Superlum, Cork, Ireland) operating at 840 ± 25 nm. The detector was an

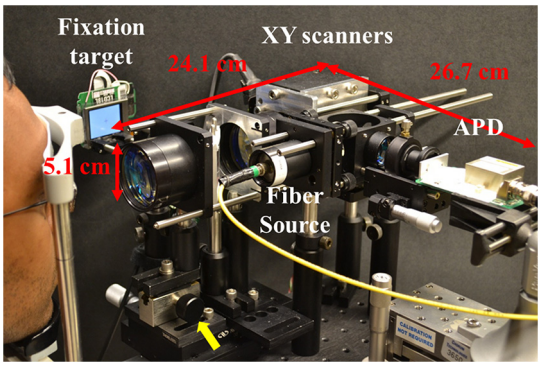

Fig. 6 Physical implementation of the described cSLO design with subject at left. The focus adjustment knob is denoted by a yellow arrow.

APD (Hamamatsu, Shizuoka-ken, Japan) with fixed gain and a custom amplifier (40-dB gain and 2.75-MHz BW) was designed and used to amplify the detector signal such that the maximum signal amplitude from the retina plus that from lens reflections filled the dynamic range of the digitizer. The digitizer used was an NI PCI 6115 card (12 bit, 10 MS/s/ch) (National Instruments, Austin, Texas), and scanners were controlled separately with an NI PCI 6711 card (12 bit, 1 MS/s/ch) (National Instruments, Austin, Texas).

Raw images acquired with the PCI 6115 digitizer have a bit-depth of 12 bits (4096 gray levels); however, after background subtraction the resulting image bit-depth was normally reduced to ~11 bits (2048 gray levels). The resulting bit-depth for low-reflectivity eyes (~25% to 50% reflectivity of normal) was reduced to ~9 to 10 bits (512 to 1024 gray levels). We were satisfied with this trade-off between dynamic range and background subtraction, but alternatively one could forgo background subtraction and let the lens reflections saturate the detector to avoid reducing the bit-depth of the retinal image. This could be done by using a higher-gain detector, applying a higher-gain amplifier, or reducing the dynamic range of the digitizer (possible with the PCI 6115 card).

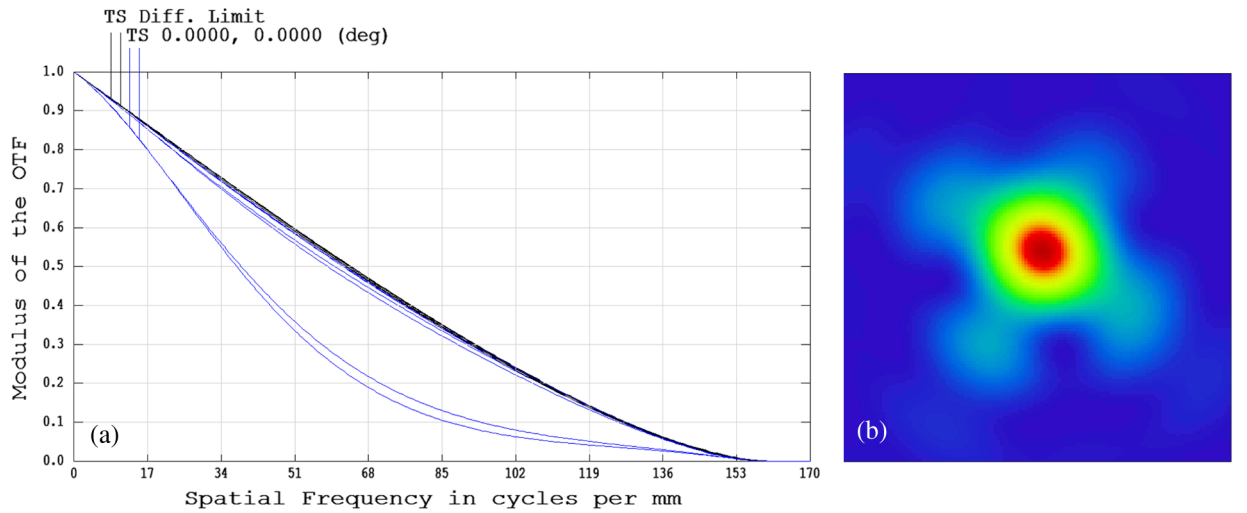

Fig. 5 (a) Modulation transfer function (MTF) of the cSLO for configurations spanning 20-deg FOV on the retina. The black curve represents the diffraction limited MTF and the blue curves represent the MTFs for nine configurations spanning a 20 deg FOV on the retina. (b) Point-spread function (PSF) of the cSLO at the retina for one of the outermost configurations. The largest full width at half maximum (FWHM) across the diagonal of the PSF was 7 μm and the box containing the PSF was 32×32 μm^2. The PSF appears different from the spot diagrams shown in Fig. 4 because in the Zemax® optical design software, the PSF takes into account diffraction while spot diagrams do not.

Custom software was developed in Labview (National Instruments, Austin, Texas) for image acquisition, scanner control, background subtraction, image dewarping, image interweaving, and gamma correction. Images were dewarped and linearly resampled due to the sinusoidal waveform of the resonant (fast) scanner. Image processing was done in real time with Matlab (Mathworks, Natick, Massachusetts) to provide correctly oriented, gamma-corrected images at 8 fps. The steps of background subtraction, dewarping, image interweaving, and gamma correction are illustrated with sample data in Fig. 7. Gamma correction was applied to enhance the contrast of features with intensity values closely spaced on a linear scale. The gamma correction algorithm used was

$$g(x,y) = f(x,y)^{\gamma}, \tag{6}$$

where $f(x,y)$ is the normalized original image's pixel intensity as a function of position, γ is the gamma value applied for gamma correction, and $g(x,y)$ is the gamma-corrected image's pixel intensity as a function of position.[32]

Image sharpness was quantitatively measured with a simple variation of the image focus measurement technique by Kautsky et al.,[33] which is computed as the ratio of the L2 norm of the high-passed image region and the L2 norm of the low-passed image region as shown in Eq. (7). We explain our method for separating a given image region into high- and low-passed image regions in Sec. 3. The overall throughput was calculated by taking the sum of the pixels in the image region of interest as shown in Eq. (8):

$$\text{Sharpness Metric} = \frac{\|\text{Im}_{\text{HP}}\|_2}{\|\text{Im}_{\text{LP}}\|_2}, \tag{7}$$

$$\text{Overall Throughput} = \sum_{i=1}^{n}\sum_{j=1}^{m} \text{Im}(i,j). \tag{8}$$

3 Results

Single-frame cSLO images of a normal human subject for two FOVs (20 and 6.7 deg) and two digitally zoomed-in FOVs (3.3 and 1.3 deg) from an original 6.7-deg FOV image are shown in Fig. 8. The relative location of a retinal image is given by the eccentricity which is defined as the distance in degrees between the fovea and the center of the image. All images exhibited minimum corneal reflection and, after background subtraction, minimum lens reflections. Imaging was done in slightly dimmed lighting with nondilated pupils (~3 mm in diameter) and with an incident power at the eye of 580 μW, which is below the maximum permissible radiant power for SLOs at 840-nm wavelength.[34]

Larger pinhole sizes were used to image larger FOVs when image resolution was limited by the sampling rate as opposed to

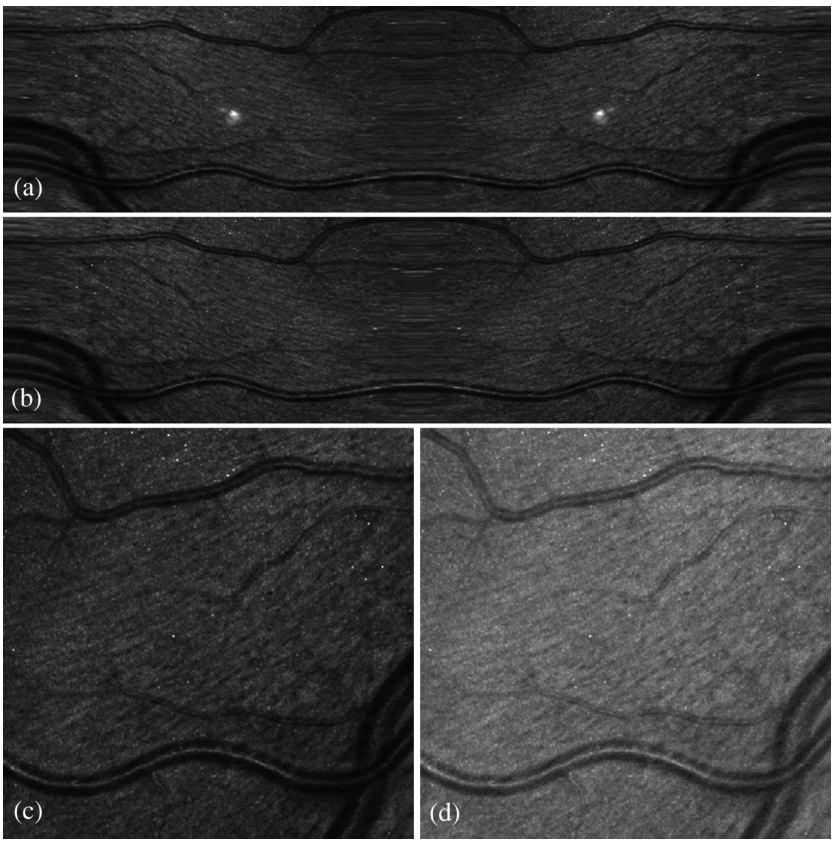

Fig. 7 Image processing steps for cSLO image acquisition on a 6.7-deg FOV image. (a) Raw image containing both forward and backward sweeps of the resonant scanner. The lens reflections appear saturated because they are the brightest features in the image, and the image was normalized to enhance visualization of darker parts of the image. (b) Raw image after background subtraction. (c) Raw image after background subtraction, dewarping, and interweaving image from both resonant scanner sweeps into a single image. (d) Image in part (c) after gamma correction with $\gamma = 0.5$ showing nerve fiber bundles.

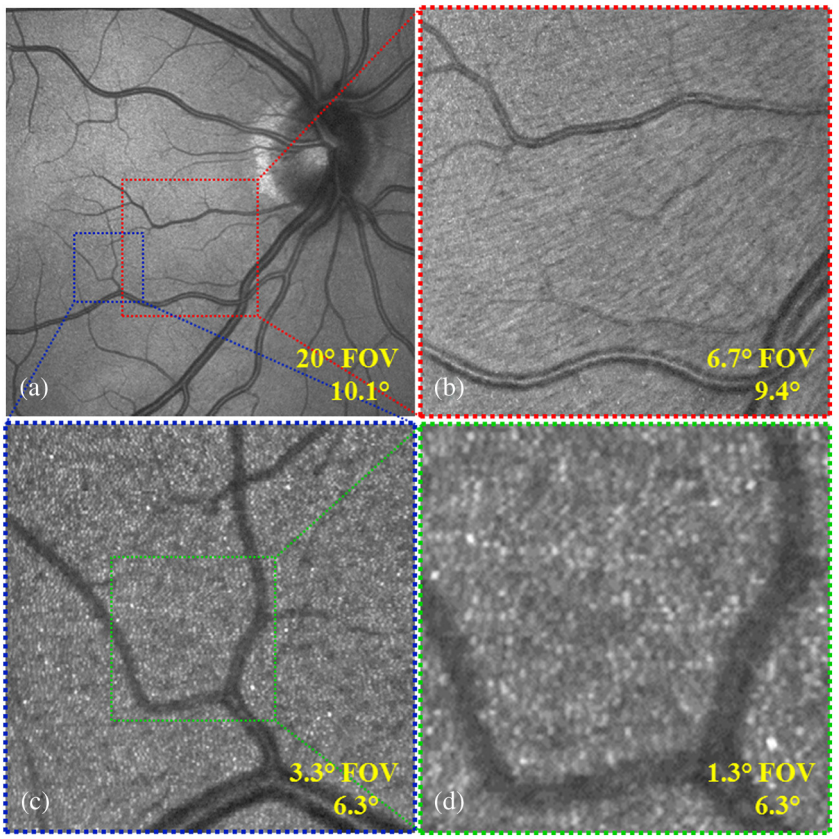

Fig. 8 Unaveraged retinal cSLO images (single frame each) from the described design at two optically zoomed in FOVs: 20 and 6.7 deg as shown in (a) and (b), respectively. The 3.3- and 1.3-deg FOV images in (c) and (d), respectively, were digitally zoomed from a 6.7-deg optically zoomed image and showed the cone photoreceptor mosaic. (a), (c), and (d) were focused on the photoreceptor layer and (b) was focused on the nerve fiber layer. Image eccentricities are given in degrees under the FOV for each image.

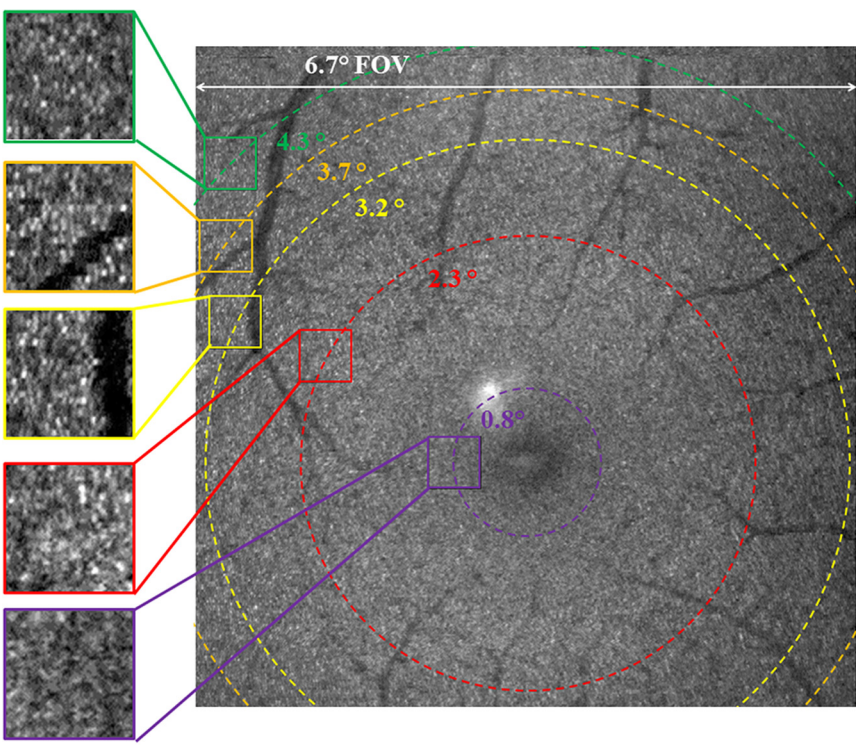

Fig. 9 A 6.7-deg FOV cSLO image of the fovea showing resolution of cone photoreceptors at retinal eccentricities $\geq \sim 3.2$ deg. The large image is a single, un-averaged frame without background subtraction taken at 8 fps with a pinhole of 30-μm diameter or a times-diffraction-limited spot size (TDL) of 1. The cropped images span a 0.5-deg FOV.

the optical resolution. We describe pinhole size in terms of the times-diffraction-limited spot size (TDL), which is the pinhole size normalized with respect to the Airy disc diameter of the collection optics (TDL = pinhole size/Airy disc diameter). A 100-μm pinhole (TDL = 3.31) was used for acquiring 20-deg FOV images since the resolution for that FOV was ultimately limited by the number of lines per frame and sampling rate of our digitizer. A 20-μm (TDL = 0.66) and 30-μm (TDL = 1.0) pinhole were used for obtaining 6.7-deg FOV images because the resolution for that FOV was optically limited and those pinhole sizes provided a good balance of resolution and SNR. Images were taken at 8 fps with 500 lines per frame and a pixel density of 1000 samples per line.

In the second set of experiments shown in Fig. 9, a 6.7-deg FOV foveal image was taken with a 30-μm pinhole (TDL = 1.0), and five 0.5-deg square FOV patches at 0.8-, 2.3-, 3.2-, 3.7-, and 4.3-deg eccentricity from the foveal center were digitally zoomed to qualify how close to the fovea photoreceptors were resolved, which appeared to be at retinal eccentricities $\geq \sim 3.2$ deg.

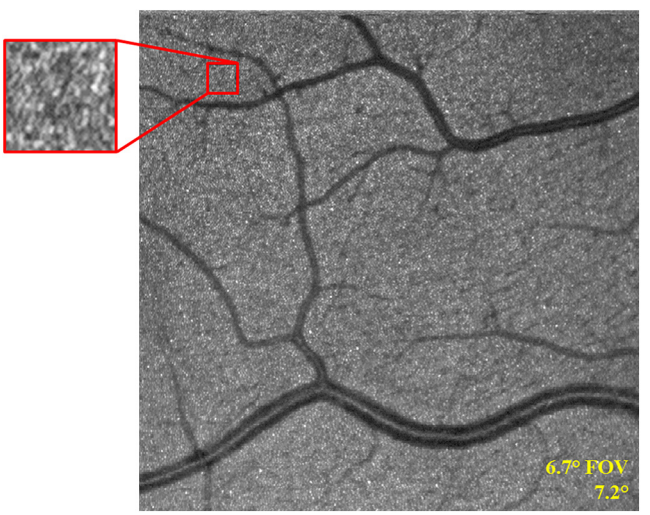

Fig. 10 The location of the portion of the retina utilized for the sharpness metric across varying TDL spot sizes is shown by the red box marked in this 6.7-deg FOV image and is at approximately 4.2 deg eccentricity. This image was taken with a TDL of 1.3 and at a 7.2-deg eccentricity.

In the third set of experiments, to determine the effect of the confocal pinhole on throughput and sharpness, five images containing a 0.4-deg area of the retina at 4.2-deg eccentricity of a subject's right eye was imaged with 6.7-deg FOV (see Fig. 10) for each of seven pinhole sizes. Pinhole sizes ranged from 10 to 100 μm in diameter with TDLs from 0.33 to 3.31. Image sharpness was quantified for each of the 0.4-deg areas using the image focus measurement technique as described previously [see Eq. (7)]. The filter used to separate the image region into low- and high-passed image regions was Gaussian with a 50% cutoff at the spatial frequency $1/12.2$ μm^{-1}. Spatial frequency was calculated by assuming the eye's second nodal point is approximately 16.5 mm from the retina,[35] which implies that a 1-deg retinal region would be approximately 288 μm wide. Since the average cone spacing at 4.2-deg eccentricity is at a higher spatial frequency [$\sim 1/8$ μm^{-1} (Ref. 36)] than the 50% spatial frequency cutoff of our filter ($1/12.2$ μm^{-1}), we expect higher values of sharpness (at the expense of throughput) as the contrast and resolution of our system improves through the use of smaller pinhole sizes. The plot of the sharpness measurements and the observed throughput is shown in Fig. 11.

Finally, we compared the imaging results of our optimized cSLO design to that of a commercial cSLO system, the Heidelberg Spectralis (Heidelberg Engineering, Inc., Vista, California, USA). With our optimized cSLO design, both 20- and 6.7-deg FOV images were taken at 8 fps with 500×1000 pixels per image. With the Heidelberg Spectralis, 20- and 15-deg FOV images were taken at 6.8 fps with 1024×1024 pixels per image and 8.8 fps with 768×768 pixels per image, respectively, using Heidelberg's "High-resolution" setting. We would like to note that a 6.7-deg FOV with the Spectralis is not possible so the 15-deg FOV setting, which is the lowest FOV setting on the Spectralis, was used instead. Results from the comparison are shown in Fig. 12.

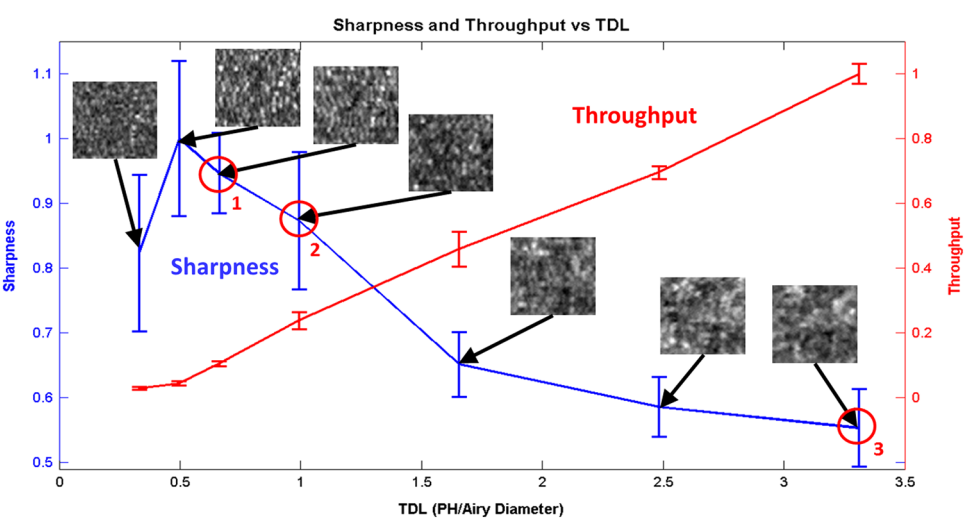

Fig. 11 Plot of sharpness and throughput for varying TDLs at the location specified in Fig. 10. Red circles delineate TDLs used for retinal imaging outside of this experiment. Red circles with subscripts 1 and 2 correspond to TDLs 0.66 and 1.0, respectively, and were used to image at low FOVs where resolution was determined by optical resolution. The red circle with subscript 3 corresponds to a TDL of 3.31 and was used to image at high FOVs where resolution was determined by digital sampling frequency not optical resolution.

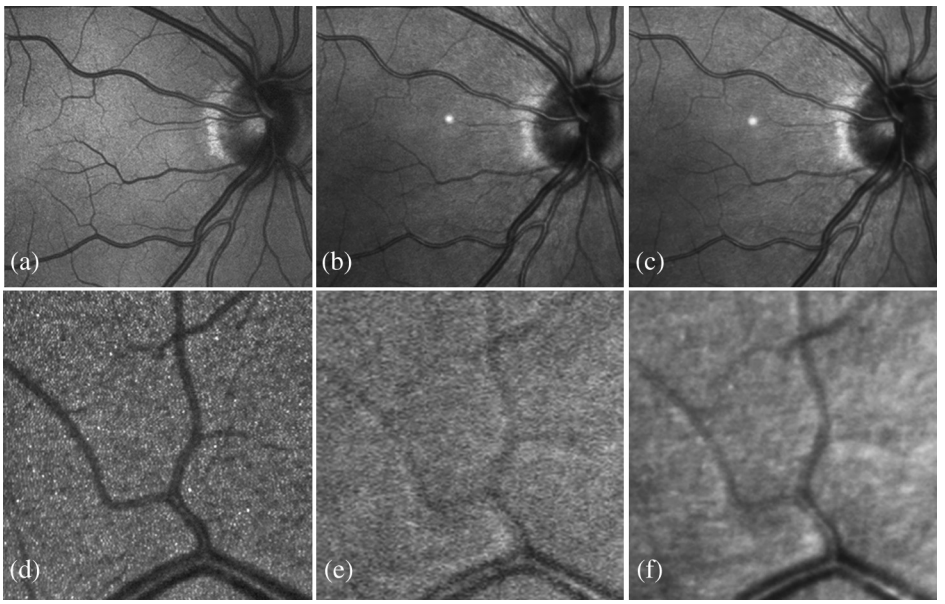

Fig. 12 Comparison of images from our optimized cSLO design and a commercially available cSLO (Heidelberg Spectralis). (a), (b), and (c) each show an 18.5-deg FOV image cropped from a 20-deg FOV image. (a) Single frame from our optimized cSLO design. (b) Single frame from the Spectralis. (c) One-hundred-frame average from the Spectralis. (d), (e), and (f) each show a 3.3-deg FOV image taken at a 6.3-deg eccentricity. (d) Single frame from our optimized cSLO design cropped from a 6.7-deg FOV image. (e) Single frame from the Spectralis cropped from a 15-deg FOV image. (f) One-hundred-frame average from the Spectralis cropped from a 15-deg FOV image.

4 Discussion

We have demonstrated a simple, compact optical design for a cSLO that produces near diffraction-limited illumination on the retina across a 20-deg FOV with minimized imaging artifacts. With the experimental implementation of our design, we demonstrated fast, high-SNR, high-resolution retinal imaging to visualize micron-scale anatomical structures of the retina *in vivo*. At lower FOVs, by adjusting the focus to the respective retinal layers, we were able to visualize nerve fiber bundles throughout the retina and photoreceptors at eccentricities $\geq \sim 3.2$ deg with TDLs ≤ 1, without the use of adaptive optics. The theoretical resolution of our system (7 μm) supports the resolution of detected individual cone photoreceptors starting at approximately 3-deg eccentricity.[36] In practice, we were able to visualize photoreceptors near this eccentricity (see Fig. 9).

Using various pinhole sizes, we quantified the relationship between the retinal image sharpness and the TDL. Experimental sharpness measurements (see Fig. 11) showed that as the confocal pinhole decreased in size, image sharpness increased while throughput decreased. However, pinholes smaller than 0.5 TDL resulted in very low SNR so sharpness appeared to decrease rather than increase.

Through an experiment comparing our optimized cSLO design to the Heidelberg Spectralis, we have shown that our design demonstrates an improvement in both image quality and resolution. This improvement is especially noticeable at a 6.7-deg FOV, in which our system can resolve parafoveal cone photoreceptors in a single frame, which is not possible with either a single frame or a 100-frame average via the Spectralis.

While adaptive optics based cSLO designs have superior resolution, this comes at the expense of cost, size, and system complexity. We have demonstrated high-quality retinal imaging of micron-scale anatomical features of the retina with a significantly more compact and affordable cSLO. Our optimized optical design for the cSLO may also be extended to OCT systems, in which the sample arm optics are nearly identical to cSLO optics.

Acknowledgments

We acknowledge Justin Migacz for his contribution to the custom amplifier used in this cSLO design. This work was supported in part by the John Chambers Fellowship (FL), NSF Grant CBET 0933059, NIH Grants R01EY014743, R21 EY02132, and R21 EY019411, and the North Carolina Biotechnology Center, IDG 2012-1015.

References

1. R. H. Webb, G. W. Hughes, and F. C. Delori, "Confocal scanning laser ophthalmoscope," *Appl. Opt.* **26**(8), 1492–1499 (1987).
2. R. H. Webb, G. W. Hughes, and O. Pomerantzeff, "Flying spot TV ophthalmoscope," *Appl. Opt.* **19**(17), 2991–2997 (1980).
3. R. H. Webb and G. W. Hughes, "Scanning laser ophthalmoscope," *IEEE Trans. Biomed. Eng.* **BME-28**(7), 488–492 (1981).
4. A. E. Elsner et al., "Reflectometry with a scanning laser ophthalmoscope," *Appl. Opt.* **31**(19), 3697–3710 (1992).
5. W. N. Wykes, A. A. E. Pyott, and Y. G. M. Ferguson, "Detection of diabetic retinopathy by scanning laser ophthalmoscopy," *Eye* **8**(4), 437–439 (1994).
6. A. Manivannan et al., "Clinical investigation of an infrared digital scanning laser ophthalmoscope," *Br. J. Ophthalmol.* **78**(2), 84–90 (1994).
7. S. Wolf et al., "Retinal hemodynamics using scanning laser ophthalmoscopy and hemorheology in chronic open-angle glaucoma," *Ophthalmology* **100**(10), 1561–1566 (1993).
8. P. S. Prasad et al., "Ultra wide-field angiographic characteristics of branch retinal and hemicentral retinal vein occlusion," *Ophthalmology* **117**(4), 780–784 (2010).
9. S. Schmitz-Valckenberg et al., "Combined confocal scanning laser ophthalmoscopy and spectral-domain optical coherence tomography imaging of reticular drusen associated with age-related macular degeneration," *Ophthalmology* **117**(6), 1169–1176 (2010).
10. Y. Tao, S. Farsiu, and J. Izatt, "Interlaced spectrally encoded confocal scanning laser ophthalmoscopy and spectral domain optical coherence tomography," *Biomed. Opt. Express* **1**(2), 431–440 (2010).

11. A. Roorda et al., "Adaptive optics scanning laser ophthalmoscopy," *Opt. Express* **10**(9), 405–412 (2002).
12. M. Pircher et al., "Simultaneous imaging of human cone mosaic with adaptive optics enhanced scanning laser ophthalmoscopy and high-speed transversal scanning optical coherence tomography," *Opt. Lett.* **33**(1), 22–24 (2008).
13. D. X. Hammer et al., "Adaptive optics scanning laser ophthalmoscope for stabilized retinal imaging," *Opt. Express* **14**(8), 3354–3367 (2006).
14. A. Dubra et al., "Noninvasive imaging of the human rod photoreceptor mosaic using a confocal adaptive optics scanning ophthalmoscope," *Biomed. Opt. Express* **2**(7), 1864–1876 (2011).
15. A. R. Wade and F. W. Fitzke, "In vivo imaging of the human cone-photoreceptor mosaic using a confocal laser scanning ophthalmoscope," *Lasers Light Ophthalmol.* **8**(3), 129–136 (1998).
16. M. Pircher et al., "Retinal cone mosaic imaged with transverse scanning optical coherence tomography," *Opt. Lett.* **31**(12), 1821–1823 (2006).
17. M. Pircher et al., "In vivo investigation of human cone photoreceptors with SLO/OCT in combination with 3D motion correction on a cellular level," *Opt. Express* **18**(13), 13935–13944 (2010).
18. B. Potsaid et al., "Ultrahigh speed spectral/Fourier domain OCT ophthalmic imaging at 70,000 to 312,500 axial scans per second," *Opt. Express* **16**(19), 15149–15169 (2008).
19. C. K. Sheehy et al., "High-speed, image-based eye tracking with a scanning laserophthalmoscope," *Biomed. Opt. Express* **3**(10), 2611–2622 (2012).
20. A. Gómez-Vieyra et al., "First-order design of off-axis reflective ophthalmic adaptive optics systems using afocal telescopes," *Opt. Express* **17**(21), 18906–18919 (2009).
21. S. A. Burns et al., "Large-field-of-view, modular, stabilized, adaptive-optics-based scanning laser ophthalmoscope," *J. Opt. Soc. Am. A* **24**(5), 1313–1326 (2007).
22. S. Stephen, "Optical systems for laser scanners," in *Handbook of Optical and Laser Scanning*, 2nd ed., pp. 69–132, CRC Press, Boca Raton, FL (2011).
23. H. Urey, D. W. Wine, and J. R. Lewis, "Scanner design and resolution tradeoffs for miniature scanning displays," *Proc. SPIE* **3636**, 60–68 (1999).
24. J. W. Goodman, "Analysis of two-dimensional signals and systems," in *Introduction to Fourier Optics*, 3rd ed., pp. 20, Roberts & Co, Englewood, CO (2005).
25. T. Wilson and A. R. Carlini, "Size of the detector in confocal imaging systems," *Opt. Lett.* **12**(4), 227–229 (1987).
26. Y. Zhang and A. Roorda, "Evaluating the lateral resolution of the adaptive optics scanning laser ophthalmoscope," *J. Biomed. Opt.* **11**(1), 014002 (2006).
27. B. Vohnsen, I. Iglesias, and P. Artal, "Directional light scanning laser ophthalmoscope," *J. Opt. Soc. Am. A* **22**(12), 2606–2612 (2005).
28. Y. N. Sulai and A. Dubra, "Adaptive optics scanning ophthalmoscopy with annular pupils," *Biomed. Opt. Express* **3**(7), 1647–1661 (2012).
29. T. Y. P. Chui, D. A. VanNasdale, and S. A. Burns, "The use of forward scatter to improve retinal vascular imaging with an adaptive optics scanning laser ophthalmoscope," *Biomed. Opt. Express* **3**(10), 2537–2549 (2012).
30. W. J. Donnelly III and A. Roorda, "Optimal pupil size in the human eye for axial resolution," *J. Opt. Soc. Am. A* **20**(11), 2010–2015 (2003).
31. A. V. Goncharov and C. Dainty, "Wide-field schematic eye models with gradient-index lens," *J. Opt. Soc. Am. A* **24**(8), 2157–2174 (2007).
32. R. C. Gonzalez and R. E. Woods, *Digital Image Processing*, Pearson/Prentice Hall, Upper Saddle River, NJ (2008).
33. J. Kautsky et al., "A new wavelet-based measure of image focus," *Pattern Recognit. Lett.* **23**(14), 1785–1794 (2002).
34. F. C. Delori, R. H. Webb, and D. H. Sliney, "Maximum permissible exposures for ocular safety (ANSI 2000), with emphasis on ophthalmic devices," *J. Opt. Soc. Am. A* **24**(5), 1250–1265 (2007).
35. J. W. Blaker, "Toward an adaptive model of the human eye," *J. Opt. Soc. Am.* **70**(2), 220–223 (1980).
36. D. Merino et al., "Observation of cone and rod photoreceptors in normal subjects and patients using a new generation adaptive optics scanning laser ophthalmoscope," *Biomed. Opt. Express* **2**(8), 2189–2201 (2011).